Variation in flow characteristics of overtopping waves on dike crests

van der Vegt, Niels; Warmink, Jord J.; Hofland, Bas; van Bergeijk, Vera M.; Hulscher, Suzanne J.M.H.

DOI
10.1016/j.coastaleng.2025.104772

Publication date
2025

Document Version
Final published version

Published in
Coastal Engineering

Citation (APA)
van der Vegt, N., Warmink, J. J., Hofland, B., van Bergeijk, V. M., & Hulscher, S. J. M. H. (2025). Variation in flow characteristics of overtopping waves on dike crests. *Coastal Engineering*, *201*, Article 104772. https://doi.org/10.1016/j.coastaleng.2025.104772

Coastal Engineering 201 (2025) 104772

Contents lists available at ScienceDirect

Coastal Engineering

journal homepage: www.elsevier.com/locate/coastaleng

Variation in flow characteristics of overtopping waves on dike crests

Niels van der Vegt [a,b,*], Jord J. Warmink [a], Bas Hofland [c], Vera M. van Bergeijk [d], Suzanne J.M.H. Hulscher [a]

[a] Department of Civil Engineering and Management, University of Twente, Enschede, The Netherlands
[b] HKV Consultants, Lelystad, The Netherlands
[c] Department of Hydraulic Engineering, Delft University of Technology, Delft, The Netherlands
[d] Department of Coastal Structures and Waves, Deltares, Delft, The Netherlands

ARTICLE INFO

Dataset link: https://github.com/nielsvandervegt/overtopping_variation

Keywords:
Wave overtopping
Residual analysis
Copula modeling
Flood risk
Dikes
Levees

ABSTRACT

During severe storms, waves can overtop dikes, leading to erosion of the crest and landward slope, which may ultimately result in breaching. To accurately model this erosion, the overtopping flow needs to be described in a time-dependent manner for each individual wave overtopping event. The peak flow velocity (u_{peak}) and peak flow thickness (h_{peak}) are critical boundary conditions in this context. Previous studies have shown that these flow characteristics are related to the overtopping volume, yet often propose deterministic models that overlook the variability and interdependency between these characteristics.

The goal of this study is to address these gaps by explicitly quantifying the variation and interdependence of u_{peak} and h_{peak}, using data from small-scale FlowDike experiments. We propose generalized distributions to describe the variation in these flow characteristics, with u_{peak} varying by 13% to 23%, depending on the waterside slope angle, and h_{peak} varying by approximately 20%. Furthermore, the interdependency between u_{peak} and h_{peak} is modeled using a Student-t copula ($\nu = 9.361$, $\rho = -0.497$), revealing a moderate negative correlation. This suggests that overtopping events with a high u_{peak} are less likely to have a large h_{peak}, and vice versa.

The findings of this study can be directly applied to improve models that describe the loading caused by overtopping waves and the resulting erosion. By incorporating the variation and interdependence of u_{peak} and h_{peak}, these models can provide a more detailed representation of the peak flow characteristics of overtopping waves. Furthermore, these insights can be applied to the design of wave overtopping simulators, enabling the simulation of more realistic overtopping flows by incorporating more of their natural variation.

1. Introduction

During severe storm events, high water levels and large waves may cause waves to overtop dikes. With each overtopping wave, water flows over the dike crest and along the landward slope which can cause erosion that can ultimately lead to a breach. The significance of this way of breaching is evident in past storm events, notably during the North Sea flood of 1953 and Hurricane Katrina in 2005. In both events, the majority of breaches resulted from erosion caused by overtopping waves (ILIT, 2006).

A key challenge for coastal engineers is designing the dike crest height to meet safety standards defined by a target probability of flooding. This is typically achieved by modeling the erosion of grass and clay on the crest and landward slope due to overtopping waves (Dean et al., 2010; van der Meer et al., 2011; Hughes, 2011; van Bergeijk et al., 2021). For these erosion models, the hydraulic loading imposed by overtopping waves must be determined along the crest and landward slope. This loading is often expressed in terms of flow velocity and flow thickness (Schüttrumpf and Oumeraci, 2005; van Bergeijk et al., 2019), but may also include shear stresses, normal stresses, pressures, and flow detachment (Ponsioen et al., 2019; van Bergeijk et al., 2022). When applying these models, flow characteristics such as the peak flow velocity (u_{peak}) and peak flow thickness (h_{peak}) at the waterside crest line of the dike are used as input, making accurate predictions at this location essential.

Over the past decades, several studies focused on predicting the u_{peak} and h_{peak} at the waterside crest line. Generally, there are two common methods. The first method estimates the 2% exceedance value of these peak flow characteristics based on the difference between the 2% wave run-up height and the freeboard (van Gent, 2002; Schüttrumpf and Oumeraci, 2005; Bosman et al., 2009; van der Meer et al.,

* Corresponding author at: Department of Civil Engineering and Management, University of Twente, Enschede, The Netherlands.
E-mail address: N.vanderVegt@utwente.nl (N. van der Vegt).

https://doi.org/10.1016/j.coastaleng.2025.104772
Received 28 February 2025; Received in revised form 2 May 2025; Accepted 6 May 2025
Available online 22 May 2025

2011, 2012; Formentin et al., 2019). The second method estimates the expected value of these peak flow characteristics based on the individual overtopping volume (V_T) (van der Meer et al., 2011; Hughes, 2017; Altomare et al., 2020).

The relations from both methods predict the marginal expected values for u_{peak} and h_{peak} without accounting for their interdependency. Hughes et al. (2012) examined the dependency between $u_{peak,2\%}$ and $h_{peak,2\%}$ and found that the 2% peak characteristics do not occur within the same overtopping event. Instead, for the overtopping event in which $u_{peak,2\%}$ was observed, the corresponding h_{peak} was relatively low, and vice versa. For breakwaters, Mares-Nasarre et al. (2019) analyzed the statistics of $u_{peak,2\%}$ and $h_{peak,2\%}$ and concluded that they were related but found no dependency between $u_{peak,2\%}$ and $h_{peak,2\%}$ for the same overtopping volume. More recently, Mares-Nasarre et al. (2024) applied a Gaussian copula to model the interdependency between the absolute dimensionless values of u_{peak} and h_{peak} for breakwaters, finding a moderate positive correlation.

The variation and interdependency of peak flow characteristics for dikes remain insufficiently quantified. Previous studies have mainly analyzed the absolute, dimensionless values of u_{peak} and h_{peak}, using 2% exceedance values. However, focusing on a single exceedance probability overlooks their full interdependency. With the shift toward erosion modeling, it becomes necessary to probabilistically evaluate erosion from each overtopping wave rather than relying solely on characteristic values. This requires a time-dependent description of the overtopping flow (Suzuki et al., 2020), whereby u_{peak} and h_{peak} are important parameters. As a result, any uncertainties or interdependencies are critical, as it can significantly affect erosion rates. Accurate modeling of their variation and interdependency is therefore essential, since relying only on marginal distributions may result in unrealistic representations of overtopping events.

The goal of this study is to quantify and model the variation and interdependency of the peak overtopping flow characteristics u_{peak} and h_{peak} at the waterside crest line of a dike. Unlike previous studies, we assess these parameters conditionally on the individual overtopping volume (V_T). We apply residual analysis to capture the variability of u_{peak} and h_{peak} given V_T and use copula modeling to examine their interdependency. The findings provide a more accurate prediction of the natural variability of u_{peak} and h_{peak} at the crest of a dike, thereby enhancing the time-dependent description of overtopping flow.

The paper is organized as follows: in Section 2 we present the used data from the FlowDike experiments (Lorke et al., 2012b). First, we quantify the variation in u_{peak} and h_{peak} and propose generalized distributions using residual analysis in Section 3. Next, we investigate their interdependency by determining the best-fitting copula in Section 4. Then, in Section 5, we integrate the generalized distributions and copula to develop a model that captures both variation and interdependency. Finally, we discuss the results in Section 6 and present our conclusions in Section 7.

2. Experimental data

2.1. FlowDike experiments

In this study we use data from the FlowDike experiments (Lorke et al., 2012b,a). These small-scale experiments were conducted to investigate the effects of current and wind on wave run-up and overtopping. During the test, extensive measurements were conducted. The tests were performed in a shallow water basin (LxWxD = 35 m x 25 m x 0.9 m) at the Danish Hydraulic Institute.

On one side of the basin, 36 paddles were installed to generate multidirectional waves, while a dike was constructed on the opposite side. The dike consisted of two segments with dike crests of 70 cm and 60 cm above the basin bottom, respectively. A schematic of the experimental setup is shown in Fig. 1. A total of 24 experiments were conducted on a dike with a 1:3 waterside slope and 32 on a dike with a 1:6 waterside slope, varying in the presence or absence of current and wind, wave conditions and obliqueness.

Using eight of these experiments, Hughes and Thornton (2016) created a dataset with time series of 5799 individual overtopping events based on the measurements on the 60 cm high dike. These eight experiments were conducted with normally incident waves without current or wind to avoid their influence. In this study, we will use the same eight experiments to solely study the variation in peak flow velocity and thickness without additional effects. The dataset for this study is provided by Steven Hughes, the characteristics of these eight experiments are summarized in Table 1. For details on the derivation of this dataset, refer to Hughes (2015).

2.2. Wave overtopping events

During the FlowDike experiments, Lorke et al. (2012a) measured the flow velocity (u) at the waterside crest line of the dike using micro-propellers, and the flow thickness (h) using gauges, see Fig. 2. Hughes and Thornton (2016) used the time series from these experiments to extract the individual overtopping waves. For each overtopping wave, the peak values of the flow velocity (u_{peak}) and thickness (h_{peak}) are defined as the measured maximum values. Additionally, they calculated the total individual overtopping volume per meter width (V_T) by multiplying the time series of u and h and integrating the result with respect to time. For more details on this data collection, refer to Hughes (2015).

In this study, the obtained peak flow characteristics u_{peak} and h_{peak} will be used to assess the variation in overtopping flow characteristics. Often, these peak flow characteristics are either related to the wave run-up height (R_u) or the individual overtopping volume per meter (V_T). Although both are measured during the FlowDike experiments, the distance between the run-up gauge and the slope was too large, resulting in part of the wave run-up event missing (den Bieman et al., 2024). Therefore, it is opted to only assess the variation conditional to V_T.

Since the flow characteristics are derived from experimental data, this variation may be partly attributed to measurement error. Lorke et al. (2012a) reports the accuracy of the micro-propeller to be 2%. The gauges on the crest of the dike were calibrated at the beginning of the day. Although the accuracy is not explicitly reported, gauges typically have an accuracy in the range of a few percent. This especially could affect the overtopping events with a low overtopping volume and cause outliers in the analysis. Therefore, it is decided to filter all events with a peak flow thickness lower than 1 cm from the dataset (449/5799 events).

In the top four figures of Fig. 3, u_{peak} and h_{peak} are plotted against V_T. This figure shows that the variation is considerable and larger than the measurement error, suggesting that other sources contribute to the observed variation.

2.3. Dimensionless parameters

Dimensionless quantities are used to relate results from the small-scale experiments to real-scale dikes. For this study, we made the measured flow characteristics from the dataset of Hughes and Thornton (2016) dimensionless using standard expressions based on Froude similarity (van Gent, 2002; Schüttrumpf and Oumeraci, 2005), as presented in Eq. (1).

$$u^*_{peak} = \frac{u_{peak}}{\sqrt{g H_{m0}}} \qquad h^*_{peak} = \frac{h_{peak}}{H_{m0}} \qquad V^*_T = \frac{V_T}{{H_{m0}}^2} \tag{1}$$

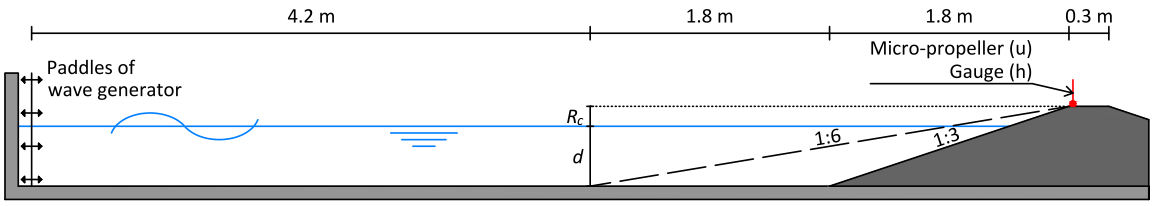

Fig. 1. Cross-section of the experimental setup during the FlowDike experiments. The dashed line indicates experiments with the 1:6 waterside slope. Position of the micro-propellor and gauge to measure u and h in red (positioned 3 cm from waterside dike crest).

Table 1
Characteristics of the FlowDike experiments used in this study, see Appendix A for the nomenclature.

Exp. ID	cot α [-]	N [m]	N_{ow} [-]	q_{avg} [l/m]	H_{m0} [m]	T_p [s]	$T_{m-1,0}$ [s]	$\xi_{m-1,0}$ [-]	d [m]	R_c [m]	f_s [Hz]
3.1 (198)	3	1004	663	1.94	0.103	1.781	1.619	2.101	0.50	0.10	25
3.2 (199)	3	1001	446	0.85	0.094	1.280	1.164	1.581	0.50	0.10	25
3.3 (200)	3	1002	814	4.78	0.150	2.156	1.960	2.108	0.50	0.10	25
3.4 (201)	3	1027	747	3.39	0.148	1.517	1.379	1.493	0.50	0.10	25
6.1 (451)	6	1058	581	0.61	0.090	1.710	1.555	1.079	0.55	0.05	40
6.2 (453)	6	1086	868	1.64	0.122	1.830	1.663	0.992	0.55	0.05	40
6.3 (456)	6	1062	892	4.28	0.157	2.130	1.936	1.108	0.55	0.05	40
6.4 (457)	6	1073	788	1.84	0.141	1.510	1.373	0.761	0.55	0.05	40

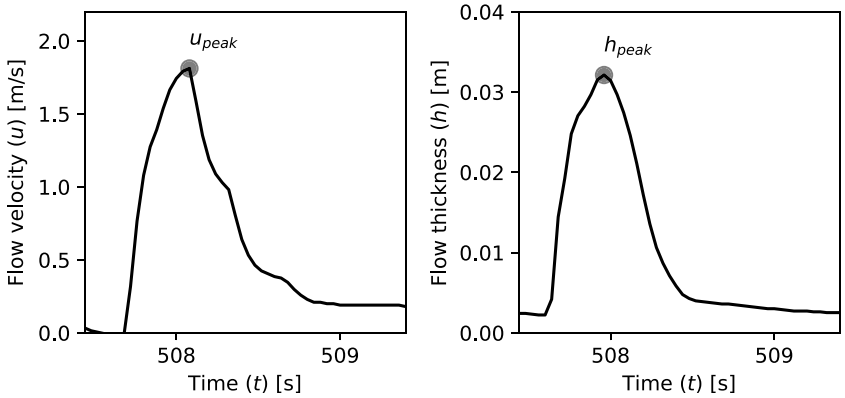

Fig. 2. Time series measurements of the flow velocity (left) and flow thickness (right) of an overtopping event on the waterside crest line during experiment 3.3. The peak flow velocity (u_{peak}) and thickness (h_{peak}) are defined as the maximum values.

3. Variation of peak flow characteristics

3.1. Expected relations of peak flow characteristics

The variation of the peak flow velocity (u_{peak}) and thickness (h_{peak}) is described through residual analysis. Within the residual analysis, we examine the differences between the observations and their expected values, known as residuals. By examining the distribution of the residuals, we gain insight into the variability. In this analysis, we utilize the dimensionless parameters u^*_{peak}, h^*_{peak}, and V^*_T.

As a first step, relations for the expected values of the dimensionless peak flow velocity ($E(u^*_{peak})$) and thickness ($E(h^*_{peak})$) need to be derived. From Fig. 3, it is observed, there is a relation between u^*_{peak}, h^*_{peak} and the dimensionless individual overtopping volume (V^*_T). Therefore, these relations for the expected values will be conditional on V^*_T, see Eq. (2).

$$E(x|V^*_T) = f_x(V^*_T) \quad x \rightarrow u^*_{peak}, h^*_{peak} \tag{2}$$

Previous studies by van der Meer et al. (2011) and Hughes (2017) demonstrated that a power-law relation provides a good fit for relating u_{peak} and h_{peak} with V_T. Following their approach, we adopt a power-law relation to describe the relation, as expressed in Eq. (3). Based on non-linear least squares the coefficients a and b in these functions were fitted on the data of each experiment separately, see Table 2. An example of these fitted functions for experiment 3.3 is presented in Fig. 4.

$$E(u^*_{peak}|V^*_T) = a_u\, V^{*\,b_u}_T \quad E(h^*_{peak}|V^*_T) = a_h\, V^{*\,b_h}_T \tag{3}$$

The goodness of fit of these fitted relations is visually assessed based on a comparison between the observed and predicted values. An example of this comparison for experiment 3.3 is presented in Fig. 4. The obtained figures show that the data are evenly scattered around the diagonal across the entire domain of u^*_{peak} and h^*_{peak}, indicating the functions predict the expected values well across the entire domain.

To quantify the variation of the scatter, the Root Mean Squared Error (RMSE) is calculated, see Eq. (4) based on the relation obtained from comparing the observed and predicted values. The RMSE is calculated per experiment for all individual overtopping events ($i = 1, \ldots, N_{ow}$).

$$\mathrm{RMSE}(x) = \sqrt{\frac{1}{N_{ow}} \sum_{i=1}^{N_{ow}} \left(x_i - E(x_i|V^*_{T,i}) \right)^2} \tag{4}$$

In Table 2, the RMSE is presented for all experiments. The results show for experiments with a 1:3 waterside slope, the RMSE of u^*_{peak} is on average larger than for the 1:6 waterside slope, implying a larger variation. The difference in variation is less for h^*_{peak} between the two slope angles, suggesting that the variation in the flow thickness is less affected by the slope angle.

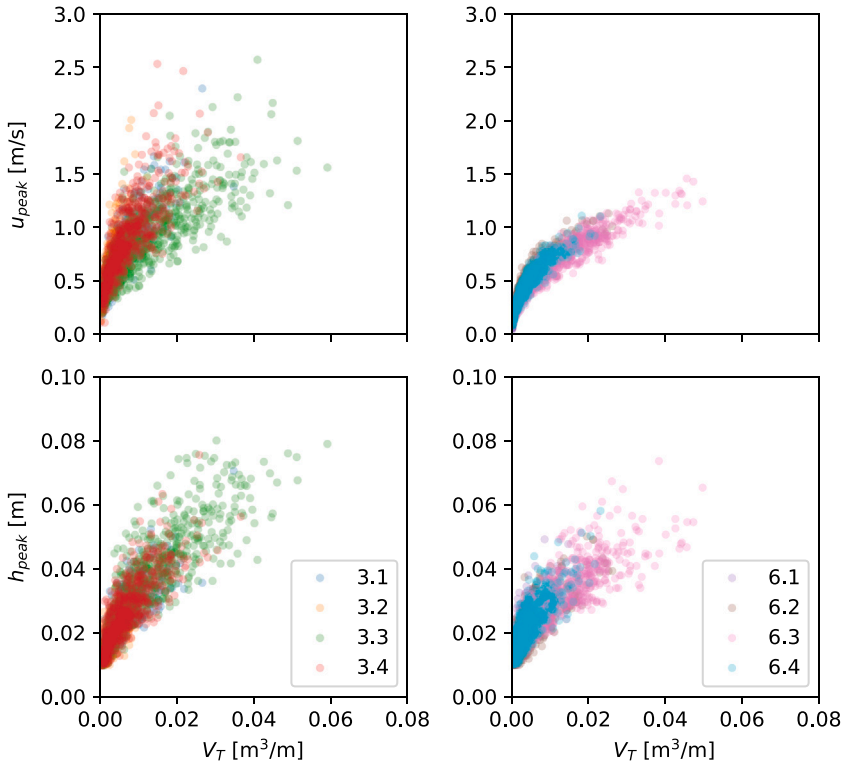

Fig. 3. Peak flow velocity u_{peak} (top) and flow thickness h_{peak} (bottom) against the individual overtopping volume (V_T) for experiments with a 1:3 waterside slope (left) and 1:6 waterside slope (right).

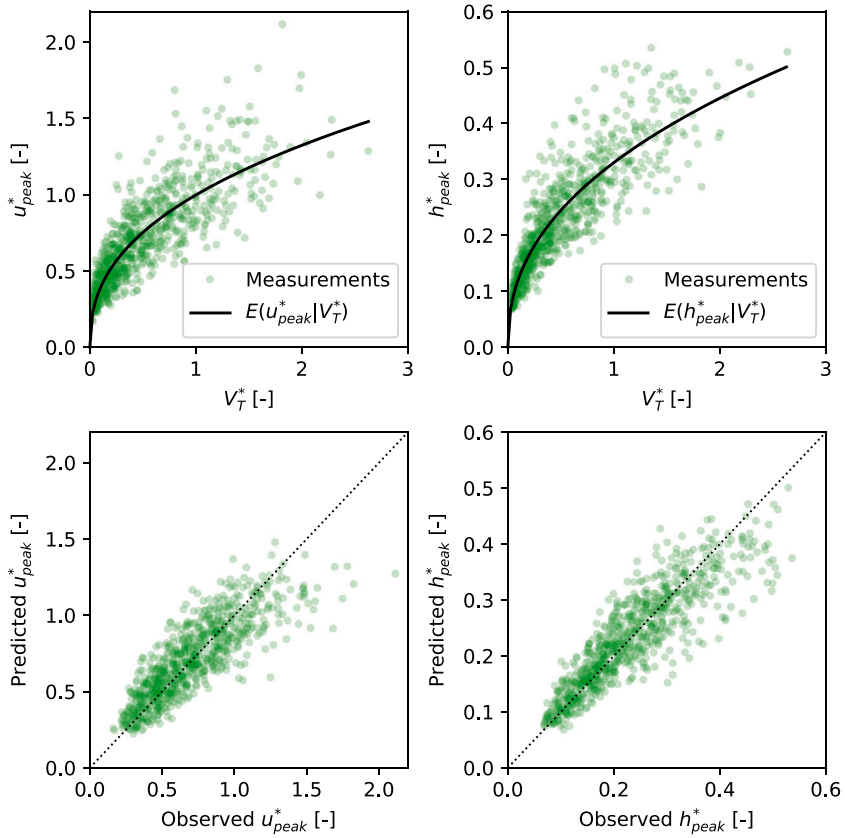

Fig. 4. Fitted relations for the expected values of u^*_{peak} and h^*_{peak} (top) and comparison between the observed and predicted u^*_{peak} and h^*_{peak} (bottom) for experiment 3.3 with a 1:3 waterside slope. For all experiments, see the supplementary figures.

Table 2
For the different experiments (denoted by ID), fitted coefficients in power-law relation for expected value of flow velocity (a_u, b_u) and flow thickness (a_h, b_h) with their root mean squared error (RMSE). The standard deviation of the fitted Normal distributions for the residuals r_u and r_h are shown, along with the D-statistics and p_{KS}-values calculated using the Kolmogorov–Smirnov test. Statistical significant fits in **bold** (p_{KS}-value > 0.05).

ID	Flow velocity (u^*_{peak})					Flow thickness (h^*_{peak})				
	a_u	b_u	RMSE	σ_u	p_{KS}-value	a_h	b_h	RMSE	σ_h	p_{KS}-value
3.1	1.017	0.452	0.142	0.195	**0.671**	0.309	0.391	0.042	0.185	**0.385**
3.2	1.334	0.538	0.153	0.223	**0.850**	0.268	0.275	0.041	0.216	**0.487**
3.3	0.998	0.408	0.166	0.228	**0.836**	0.330	0.432	0.047	0.193	**0.632**
3.4	1.226	0.420	0.164	0.225	**0.631**	0.300	0.390	0.039	0.216	**0.523**
6.1	0.671	0.467	0.037	0.131	**0.109**	0.338	0.291	0.043	0.207	**0.241**
6.2	0.789	0.413	0.056	0.136	**0.232**	0.271	0.332	0.033	0.196	**0.961**
6.3	0.790	0.451	0.058	0.121	**0.243**	0.266	0.350	0.033	0.173	**0.668**
6.4	0.821	0.442	0.046	0.129	**0.262**	0.278	0.335	0.028	0.186	**0.494**

3.2. Analysis of variations in peak flow characteristics

Using the derived relations for the expected values from the previous section, we can determine the residuals. The definition of residuals depends on the scatter. Since we observe increasing scatter in both u^*_{peak} and h^*_{peak} with increasing V^*_T (heteroscedasticity), a multiplicative model is used. In this model, the observed value is expressed as the product of the expected value and a distribution capturing the variability in the residuals, R'_x. Respectively, the distribution describing the variation of u^*_{peak} is denoted by R'_u and h^*_{peak} by R'_h. An example is shown in Eq. (5).

$$x = E(x|V^*_T) \cdot R'_x \qquad x \rightarrow u^*_{peak}, h^*_{peak} \tag{5}$$

Since the dataset contains small individual overtopping events with low values for u^*_{peak} and h^*_{peak}, an adjustment is needed as a multiplicative model can become unstable when the expected value approaches 0. To address this, we apply a transformation using $R'_x = \exp(R_x)$, see Eq. (6). This transformation assumes that the multiplicative term follows a Log-Normal distribution, and therefore R follows a Normal distribution.

$$x = E(x|V^*_T) \cdot \exp\left(R_x\right) \tag{6}$$

The distributions for R will be defined based on the residuals calculated using data from the experiments. For each overtopping event i, the residuals of u^*_{peak} and h^*_{peak}, denoted by $r_{u,i}$ and $r_{h,i}$, are calculated by expressing Eq. (6) in terms of $r_{x,i}$, as shown in Eq. (7). This results in a set of residuals for u^*_{peak} and h^*_{peak} for each experiment, denoted by r_u and r_h.

$$r_{x,i} = \ln\left(x_i\right) - \left(E(x_i|V^*_{T,i})\right) - \overline{r_x} \tag{7}$$

Since the residuals are determined using a logarithmic transformation, fitting a Normal distribution on the residuals will lead to a slight shift in the mean (± 0.05). To align all distributions at $\mu = 0.0$, a correction is applied by subtracting the mean of the residuals ($\overline{r_x}$) from each individual residual, as shown in Eq. (7). It should be noted that this correction does not affect the variance of the distribution.

The choice to apply a logarithmic transformation is evaluated by calculating the coefficient of determination (R^2) for both the non-transformed and transformed residuals. The R^2 values for the transformed residuals ($R^2_{u^*} = 0.994$; $R^2_{h^*} = 0.987$) are higher than those for the non-transformed residuals ($R^2_{u^*} = 0.982$; $R^2_{h^*} = 0.982$). Therefore, it is concluded that the transformed residuals result in a better fit than the non-transformed residuals.

Normal distributions are fitted to the residuals r_u and r_h for each experiment using Maximum Likelihood Estimation (MLE). The standard deviations (σ_u and σ_h) of these distributions are reported in Table 2. The standard deviation varies between the different experiments, this may be caused by the different experimental parameters (e.g. waterside slope, significant wave height). The dependency on the experimental parameters will be studied in the next section. An example of the binned residuals and the fitted Normal distribution for experiment 3.3 is presented in Fig. 5.

The goodness of fit of the fitted Normal distributions is statistically assessed using the Kolmogorov–Smirnov (KS) test, which evaluates whether the distribution of the residuals follows a Normal distribution (Zwillinger and Kokoska, 2019). The KS test is chosen because we are primarily interested in modeling the center of the distribution rather than the tails. The KS test provides a p_{KS}-value, where a value greater than 0.05 suggests that the data are well-approximated by a Normal distribution. For all fits on r_u and r_h, the p_{KS}-value exceeds 0.05, confirming a good fit. The p_{KS}-values are summarized in Table 2.

Furthermore, the goodness of fit is also visually assessed using quantile–quantile (Q-Q) plots. These plots illustrate how well the data are approximated by a Normal distribution across different exceedance frequencies. An example of the Q-Q plots is shown in Fig. 5. Overall, the Normal distribution provides a good fit to the data. However, in some experiments, small deviations are observed in the tails, potentially due to limitations in the measurement setup, or nonlinear flow behavior. Overall, both the KS test and Q-Q plots confirm that the residuals are well-described by a Normal distribution.

3.3. Sensitivity of variation to experimental parameters

The fitted distributions from the previous section illustrate the variation in peak flow characteristics across experiments. However, the standard deviation of the residuals r_u and r_h varies between experiments, potentially due to differences in experimental parameters. To investigate this, a trend sensitivity analysis is conducted, examining the relation between an experimental parameter and the standard deviation of the fitted distributions for both r_u and r_h (Figs. 6 and 7). The Wald test is used to assess statistical significance, with a trend considered significant if the p_W-value is below 0.05 (Fisher, 1992). Additionally, the slope of the trend line is examined to evaluate the magnitude of the change in variation (Table 3).

The dependency on the waterside slope angle is first investigated, see Fig. 6. Several studies focusing on the expected value of the peak flow velocity (u_{peak}) have proposed models dependent on the waterside slope angle α (Bosman et al., 2009; van der Meer et al., 2011, 2012; Formentin et al., 2019). Some of these studies also incorporate α in predictions for the peak flow thickness (h_{peak}) (Bosman et al., 2009; van der Meer et al., 2012; Formentin et al., 2019).

Fig. 6 and Table 3 show the waterside slope angle α has a strong effect on r_u, with steeper slopes leading to greater variation in r_u. This effect is clear and statistically significant. In contrast, the influence of α on r_h is less pronounced and not statistically significant.

In a similar manner, the dependency on the wave conditions is explored. For this analysis, the dimensionless parameters of relative freeboard (R_c/H_{m0}) and the spectral Iribarren number ($\xi_{m-1,0}$, see Eq.

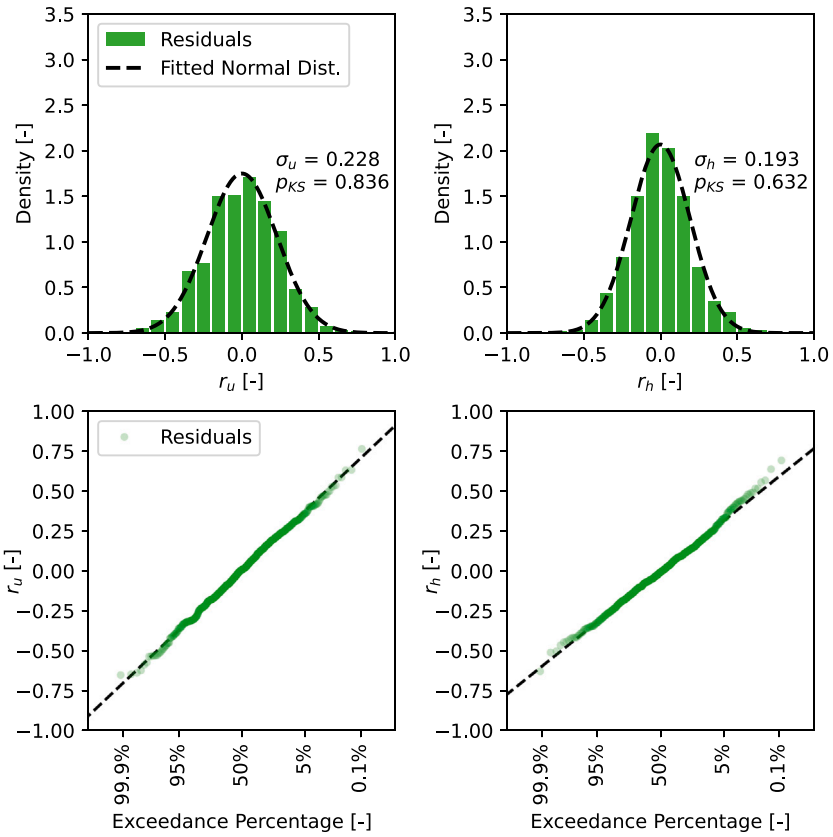

Fig. 5. Fitted Normal distributions for the residuals of r_u and r_h (top) and Quantile-Quantile plots comparing the residuals to the theoretical quantiles of the fitted Normal distributions (bottom) for experiment 3.3 with a 1:3 waterside slope. For all experiments, see the supplementary figures. σ denotes the standard deviation of the fitted distribution, and p_{KS} the p-value of the Kolmogorov–Smirnov test.

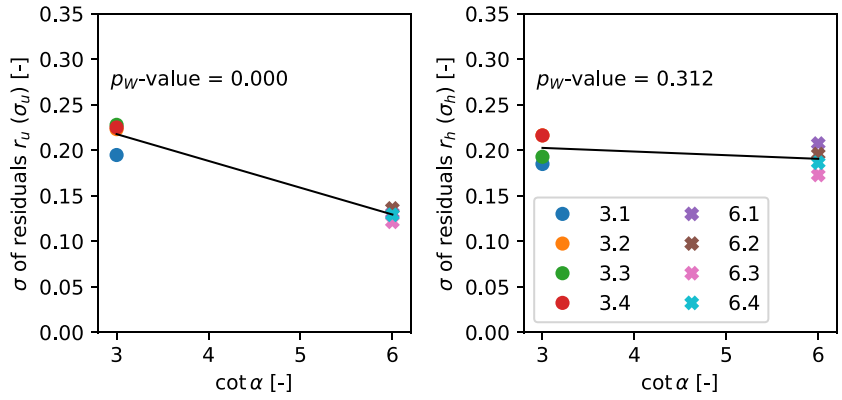

Fig. 6. Standard deviation of the residuals r_u (left) and r_h (right) for each experiment, plotted against the waterside slope angle.

(8)) are used. In Fig. 7, the trend between the these parameters and the standard deviation of the residuals r_u and r_h is presented.

$$\xi_{m-1,0} = \frac{\tan\alpha}{\sqrt{\frac{2\pi H_{m0}}{g T_{m-1,0}^2}}} \tag{8}$$

Fig. 7 shows that both the relative freeboard and the Iribarren number have little effect on the standard deviation of r_u. For the standard deviation of r_h, it is observed that a low relative freeboard ($R_c/H_{m0} < 0.5$) may lead to less variation in peak flow thickness. However, drawing conclusions from this trend is challenging, as the tested range of R_c/H_{m0} differs between experiments with 1:3 and 1:6 waterside slopes. This discrepancy, resulting from differences in water level during the experiments, complicates the interpretation of trends across the full range of R_c/H_{m0} for both slopes.

Another possible dependency is observed for the Iribarren number in relation to the variation in peak flow thickness. Fig. 7 shows that the standard deviation increases between $0.5 < \xi_{m-1,0} < 1.0$ and decreases between $1.5 < \xi_{m-1,0} < 2.0$. This may be related to the breaker type of the waves and could suggest that overtopping flows caused by plunging breakers result in larger variation in peak flow thickness.

In conclusion, the waterside slope angle is a significant explanatory variable for the variation in peak flow velocity. The relative freeboard and the Iribarren number may influence the variation in peak flow thickness, but their effect is relatively small. Therefore, it is concluded

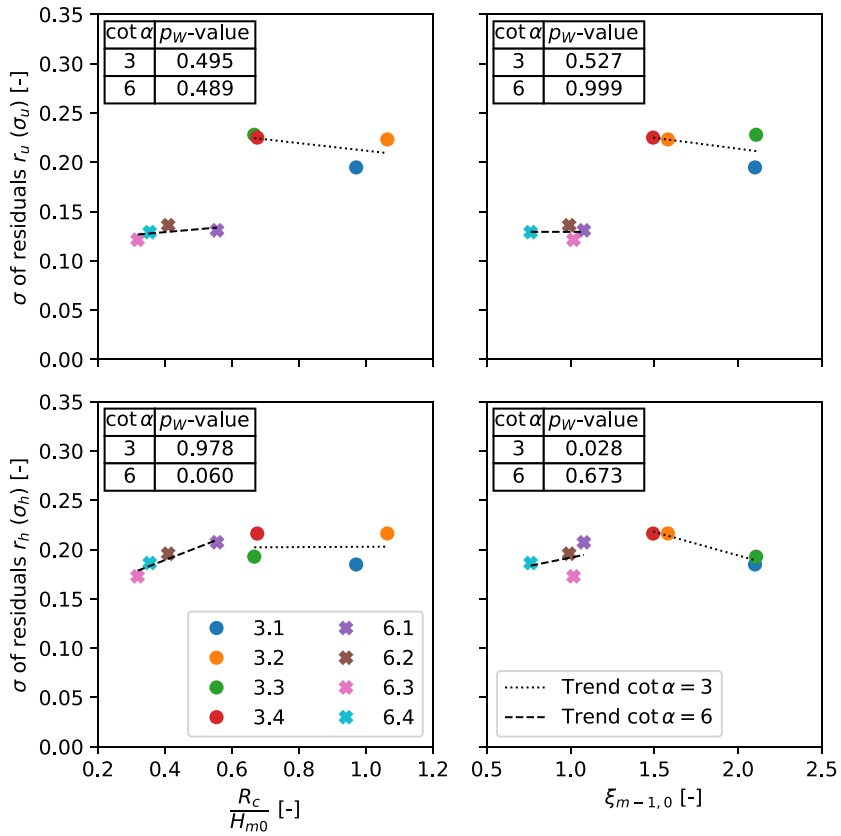

Fig. 7. Standard deviation of the residuals r_u (top) and r_h (bottom) for each experiment, plotted against the relative freeboard R_c/H_{m0} (left) and spectral Iribarren number $\xi_{m-1,0}$ (right).

Table 3
Slope of the trend line $d\sigma/dx$ and p_W-values from the Wald Test for trends between experimental parameters and residuals r_u and r_h. Statistical significant trends in **bold** (p_W-value <0.05).

Experimental parameter	cot α	r_u (σ_u)		r_h (σ_h)	
		$d\sigma/dx$	p_W-value	$d\sigma/dx$	p_W-value
cot α	–	−0.029	**0.000**	−0.004	0.312
R_c/H_{m0}	3	−0.038	0.495	−0.022	0.527
	6	0.030	0.527	0.000	0.999
$\xi_{m-1,0}$	3	0.002	0.978	−0.048	**0.028**
	6	0.132	0.060	0.034	0.673

that these experimental parameters are not a significant explanatory variable for the variation in peak flow thickness.

3.4. Generalized distributions of peak flow characteristic variation

The distributions derived in Section 3.2 are specific to their respective experiments. These distributions are combined with the dependencies identified in Section 3.3 to construct generalized distributions, R_u and R_h, similar to Eq. (6). These generalized distributions are intended to be applicable across a range of conditions.

The standard deviations of R_u (σ_u) and R_h (σ_h) must be determined to construct these generalized distributions. Based on the identified dependencies on experimental parameters, σ_u is defined as a function of the waterside slope angle α. Since no strong dependencies were found for σ_h, it is assumed to be constant and independent of experimental parameters. The values of σ_u are calculated by grouping all residuals according to the two slope angles and determining their standard deviations. For a 1:3 waterside slope, σ_u is 0.219, while for a 1:6 waterside slope, it is 0.129. In contrast, σ_h is assumed to remain constant at 0.195 across all experiments. This results in the non-dimensional generalized distributions given in Eq. (9).

$$
\begin{aligned}
u_{peak} &= E(u_{peak}|V_T) \cdot \exp\left(R_u(\alpha)\right) \\
h_{peak} &= E(h_{peak}|V_T) \cdot \exp\left(R_h\right) \\
&\text{With:} \\
R_u(\alpha) &\sim \mathcal{N}(0, \sigma_u(\alpha)^2) \\
R_h &\sim \mathcal{N}(0, {\sigma_h}^2) \\
\sigma_u(\alpha) &= \begin{cases} 0.219, & \text{if } \cot\alpha = 3 \\ 0.129, & \text{if } \cot\alpha = 6 \end{cases} \\
\sigma_h &= 0.195
\end{aligned}
\tag{9}
$$

The generalized distribution is compared against the distribution of the residuals r_u and r_h of each experiment separately. An example of this comparison for experiment 3.3 is presented in Fig. 8. The goodness of fit of the generalized distributions is statistically assessed using the Kolmogorov–Smirnov (KS) test and visually using Quantile-Quantile (Q-Q) plots.

For almost all fits, the p_{KS}-value exceeds 0.05, confirming a good fit, see Table 4. The only exception is experiment 6.3, where the p_{KS}-value is 0.048 when describing the variation in peak flow thickness. The Q-Q plots show that for this experiment, the generalized distribution provides a good fit for exceedance frequencies of 95% and lower. For larger exceedance frequencies, some deviation is observed. These correspond to waves with very small peak flow thicknesses, which are more difficult to measure and therefore more uncertain. This phenomenon is also visible to a certain extent in the Q-Q plots of other experiments, as can be seen in the supplementary figures. Overall, the Q-Q plots show that the common range, between 5% and 95%, is well predicted by the generalized model for all experiments. This provides confidence that the model can be applied to describe the variation in peak flow characteristics.

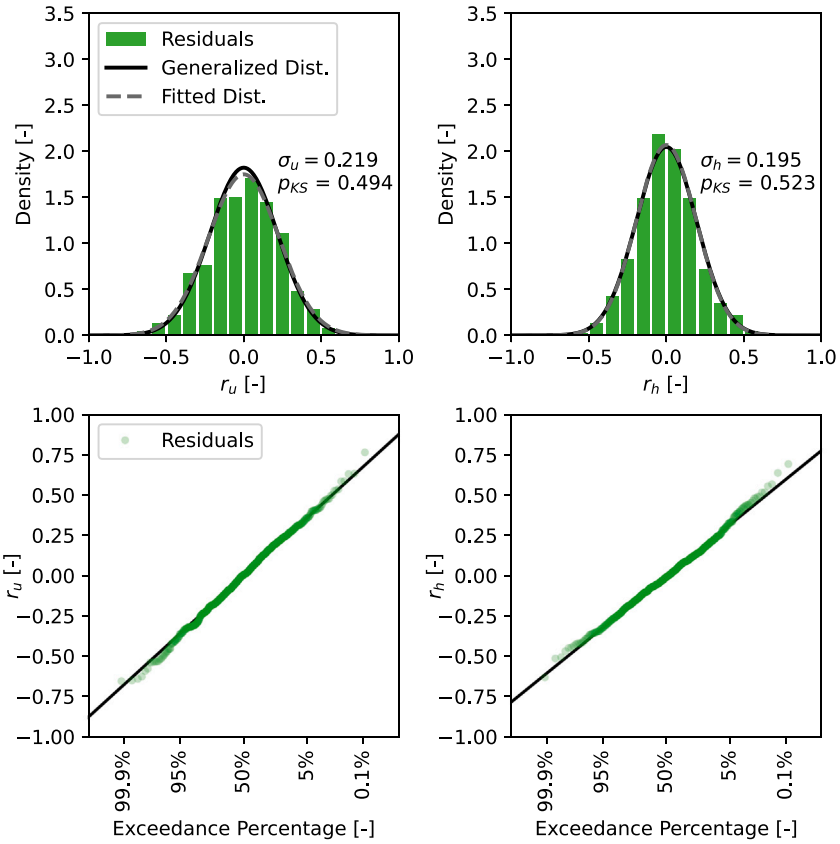

Fig. 8. Generalized distributions for the residuals of r_u and r_h (top) and Quantile-Quantile plots comparing the residuals to the theoretical quantiles of the generalized distributions (bottom) for experiment 3.3 with a 1:3 waterside slope. For all experiments, see the supplementary figures.

Table 4
For the different experiments (denoted by ID), the standard deviations of the generalized distributions for the variation of the flow velocity R_u and flow thickness R_h, along with the p_{KS}-values calculated using the Kolmogorov–Smirnov test. Statistical significant fits in **bold** (p_{KS}-value >0.05).

ID	Flow velocity (r_u)		Flow thickness (r_h)	
	σ_u	p_{KS}-value	σ_h	p_{KS}-value
3.1	0.219	**0.083**	0.195	**0.282**
3.2		**0.925**		**0.246**
3.3		**0.494**		**0.523**
3.4		**0.805**		**0.416**
6.1	0.129	**0.137**	0.195	0.048
6.2		**0.092**		**0.959**
6.3		**0.149**		**0.077**
6.4		**0.266**		**0.232**

4. Interdependencies between peak flow characteristics

4.1. Copula modeling

In the previous section, the variation of the peak flow velocity (u_{peak}) and thickness (h_{peak}) was considered independently, conditional on the individual overtopping volume (V_T). However, Hughes et al. (2012) observed that for a combination of overtopping and overflow, the most extreme overtopping events tend to exhibit either a high peak flow velocity or a large flow thickness. Ignoring this interdependency when modeling overtopping flows may lead to an overrepresentation of certain combinations, such as simultaneous small or large values of u_{peak} and h_{peak}, which are unlikely in reality. This behavior is also evident when plotting the residuals of the dimensionless peak flow velocity (r_u) against the dimensionless peak flow thickness (r_h), which reveals a moderate negative correlation, see Fig. 9.

To further study this interdependency, copula modeling is used to model the dependency structure between the residuals r_u and r_h, with a dependency on the waterside slope angle. Mares-Nasarre et al. (2024) successfully used copula modeling to describe the individual overtopping flow characteristics at rubble mound breakwaters for depth-limited breaking wave conditions, demonstrating that it is a robust and flexible solution.

In this study, the interdependency is modeled by applying a bivariate copula to model the joint distribution of r_u and r_h, as shown in Eq. (10). Copula modeling is chosen for its flexibility in capturing the joint distribution while accounting for their dependence, without making assumptions about the marginal distributions (Nelsen, 2006).

$$H(r_u, r_h) = C(\hat{F}_{r_u}(r_u), \hat{F}_{r_h}(r_h)) \tag{10}$$

In the above equation, $H(r_u, r_h)$ is the joint distribution of the log-transformed residuals r_u and r_h, and C is the copula function. The arguments $\hat{F}_{r_u}$ and $\hat{F}_{r_h}$ are the empirical cumulative distribution functions (eCDF) of the residuals r_u and r_h, respectively. In the next sections, the derivation of these eCDFs and fitting of the copula is discussed.

4.2. Empirical cumulative distribution function

Before fitting a copula, the residuals r_u and r_h need both be transformed into an uniform marginal distribution on the unit interval [0, 1]. This is done by deriving the empirical cumulative distribution functions (eCDF) of these residuals. The eCDF provides an estimation of the CDF without assuming a specific form for the distributions. This is key as the copula should only model the dependency structure between the residuals since the variation is already quantified in Section 3.4. The

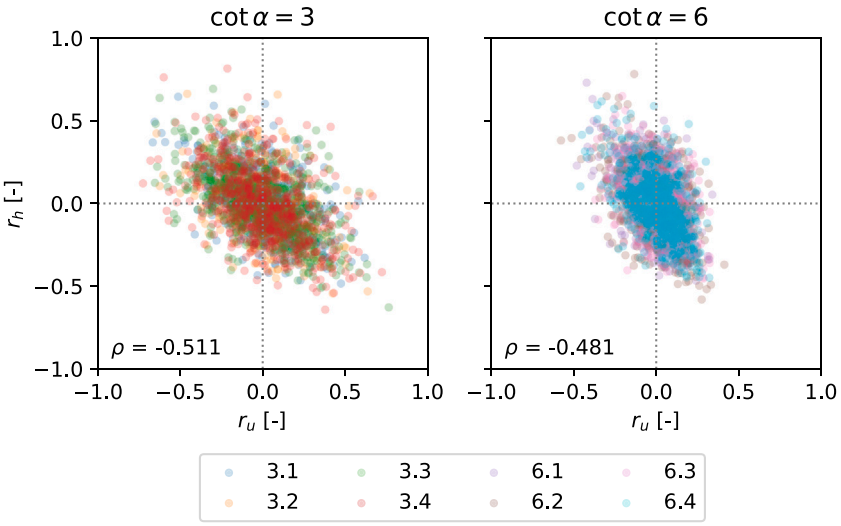

Fig. 9. Residuals r_u against r_h, color-coded by experiment, for waterside slope angles of $\cot\alpha = 3$ (left) and $\cot\alpha = 6$ (right). The Pearson correlation coefficient (ρ) is calculated for both datasets.

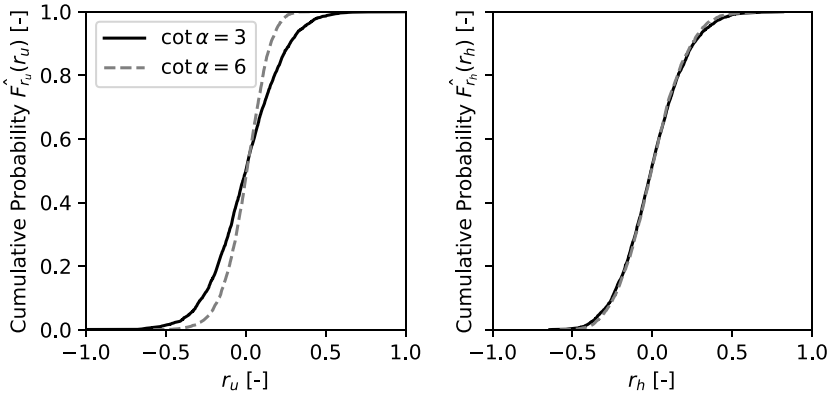

Fig. 10. Empirical cumulative distribution functions (eCDF) $\hat{F}_{r_u}$ (left) and $\hat{F}_{r_h}$ (right), grouped by the waterside slope angle α.

applied function to derive $\hat{F}_{r_u}$ and $\hat{F}_{r_h}$ is given in Eq. (11).

$$\hat{F}(r_x) = \frac{1}{N_{ow}+1}\sum_{i=0}^{N_{ow}} \mathbf{1}_{r_{x,i}\le r_x} \qquad (11)$$

$r_x \rightarrow r_u, r_h$

In this expression, $r_{x,i}$ represents the observed residual for all included overtopping events ($i = 1, \ldots, N_{ow}$), and $\mathbf{1}r_{x,i} \le r_x$ is the indicator function for the event $r_{x,i} \le r_x$. Applying Eq. (11) yields the eCDFs of r_u and r_h for both waterside slope angles, as presented in Fig. 10.

Using $\hat{F}_{r_u}$ and $\hat{F}_{r_h}$, the copula space can be constructed which consists of a 2D space between [0, 1], with each overtopping event i represented by the pair ($\hat{F}_{r_{u,i}}$, $\hat{F}_{r_{h,i}}$). This copula space is used to determine the empirical joint CDF, $\hat{F}r_u, r_h$, which estimates the cumulative probability of an event exceeding both r_u and r_h, see Eq. (12). When fitting a copula, the goal is to fit it as accurately as possible to this empirical joint CDF.

$$\hat{F}_{r_u,r_h}(r_u, r_h) = \frac{1}{N_{ow}+1}\sum_{i=0}^{N_{ow}} \mathbf{1}_{r_{u,i}\le r_u, r_{h,i}\le r_h} \qquad (12)$$

In Fig. 11, the copula space is shown. Each overtopping event i is plotted pairwise based on the cumulative probabilities $\hat{F}_{r_{u,i}}$ and $\hat{F}_{r_{h,i}}$. The color of each point is the joint cumulative probability, $\hat{F}_{r_{u,i},r_{h,i}}$, determined using Eq. (12).

4.3. Copula construction

There are several families of bivariate copulas, each suited to modeling different dependence structures. The scatter plots in Figs. 9 and 11 show no heavy tail dependency between the residuals r_u and r_h. Therefore, we chose to work with copula families that are appropriate for modeling lighter tails, specifically the Frank, Gaussian, and Student-t families (Nelsen, 2006).

All three copula families are fitted to the empirical joint CDF of the residuals r_u and r_h using the Python package *pyvinecopulib* (version 0.7.1) (Nagler and Vatter, 2024). Maximum likelihood estimation (MLE) is used for fitting each copula. To assess which copula family is the most suitable to model this dependency, we use the Akaike Information Criterion (AIC), given in Eq. (13). The AIC is commonly used for model selection because it balances the goodness of fit and complexity of the model to avoid overfitting. The goodness of fit is represented by the maximized log-likelihood $\ln(\hat{L})$, and the complexity of the model, represented by the number of coefficients of the copula family k.

$$\mathrm{AIC} = 2k - 2\ln\left(\hat{L}\right) \qquad (13)$$

The AIC provides information about which copula family is the most appropriate fit, but it does not directly quantify the statistical goodness of fit. To evaluate how well the selected copula family represents the empirical data, we apply both the Cramér–von Mises (CvM) test and the Kolmogorov–Smirnov (KS) test. The CvM test assesses the overall

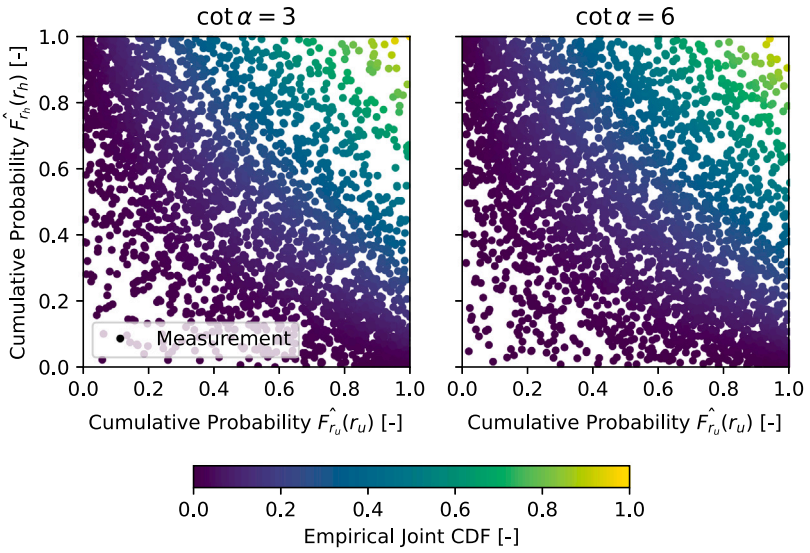

Fig. 11. Empirical joint CDF for the distribution of residuals r_u and r_h, for waterside slope angles of $\cot\alpha = 3$ (left) and $\cot\alpha = 6$ (right).

goodness of fit across the entire dependency structure, providing a p_{CvM}-value. The KS test, on the other hand, measures the maximum deviation between the empirical and theoretical copula distributions, providing a p_{KS}-value. Both a p_{CvM}-value and p_{KS}-value greater than 0.05 suggests that the dependency structure is well-approximated by the copula. Additionally, the goodness of fit of each copula is evaluated visually by comparing the cumulative probability of the empirical joint CDF ($\hat{F}$) with the cumulative probability from the copula (F). This visual assessment is useful because, for a perfect fit, these pairs should align with the diagonal.

Fig. 12 shows the three different copula families, fitted to the residuals r_u and r_h, for both waterside slope angles. In the figure, the AIC, p_{CvM}-values, and p_{KS}-values are also given. Overall, the three copulas are able to approximate the dependency structure well, indicated by the p_{CvM}-value and p_{KS}-value for each copula family is larger than 0.05. The Student-t copula has the lowest AIC and is therefore the most suitable model. Specifically, for lower cumulative probabilities ($P < 10^{-2}$), the Student-t copula provides a better estimation. This is due to the presence of moderate tail dependence in the data, as indicated by the degrees of freedom parameter ($\nu \approx 8$), which can only be captured by the Student-t copula. In contrast, the Gaussian copula accounts only for linear correlation. While the differences are small, the Student-t copula demonstrates the best overall fit for both waterside slope angles.

For both waterside slope angles, the fitted degrees of freedom parameter (ν) and correlation parameter (ρ) are relatively close to each other. The waterside slope angles seems to have no significant influence on the dependency structure. This could be explained by the fact that u_{peak} and h_{peak} are related through conservation laws, so the dependency structure remains largely unaffected. Therefore, it is sufficient to describe the dependency structure independent on the waterside slope angle. The Student-t copula is fitted again, this time on data from both waterside slopes, see Fig. 13. Therefore, we conclude a Student-t copula with a ν of 9.361, and ρ of −0.497, is well able to describe the dependency structure between r_u and r_h (p_{CvM}-value > 0.05 and p_{KS}-value > 0.05).

The fitted copula was tested for robustness using subset testing. In this approach, the dataset was randomly subsampled into 10 subsets, each containing 90% of the data. For each subset, the p_{CvM}-value and p_{KS}-value were calculated to evaluate the goodness of fit. Across the datasets, we found a p_{CvM}-value of 0.320 ($\sigma = 0.105$) and a p_{KS}-value of 0.356 ($\sigma = 0.147$). Since both average p-values are well above the threshold of 0.05, we conclude that the proposed copula demonstrates robust performance.

5. Generalized model to describe variation

Combining the generalized distributions from Section 3.4 with the Student-t copula from Section 4.3 yields a generalized model that describes the variation and interdependency of peak flow velocity and thickness. To assess how well this model captures the variation in the residuals, we compare its predictions to the scatter observed during the FlowDike experiments.

For this comparison, we examine both the joint and marginal probability distributions of the generalized model and the observed residuals for both waterside slope angles. In the generalized model, the marginal distributions follow from the generalized distributions, while the joint probability distribution is obtained by combining these distributions with the copula. For the residuals, both the marginal and joint probability distributions are estimated using kernel density estimation (KDE). The resulting distributions are presented in Fig. 14.

The goodness of fit of the generalized model is assessed visually by comparing the joint and marginal distributions of the residuals, r_u and r_h. The joint probability distribution is assessed by comparing the contour lines of the generalized model to those derived from the KDE-estimated residuals. The marginal distributions are assessed by comparing the density of the observed residuals to the generalized distributions from Section 3.4.

The generalized model appears to approximate the marginal distributions of the observed r_u and r_h well, as their probability density functions largely overlap in the top and right plots of Fig. 14. Similarly, the joint probability distribution estimated from the residuals is well-represented by the model, with contour lines following a similar shape and remaining close to each other.

Fig. 14 shows that for the 1:6 waterside slope, the contour lines deviate slightly from the generalized model at large r_h. As a result, overtopping events with relatively low peak flow velocity and large peak flow thickness tend to be slightly overestimated. This may suggest a stronger local dependence in that region. However, for the 1:3 waterside slope, this effect is not observed. The discrepancy may also be attributed to the limited sample size available to accurately capture tail behavior. Despite minor discrepancies, the generalized model successfully captures the overall variation and interdependency in r_u and r_h for both waterside slopes.

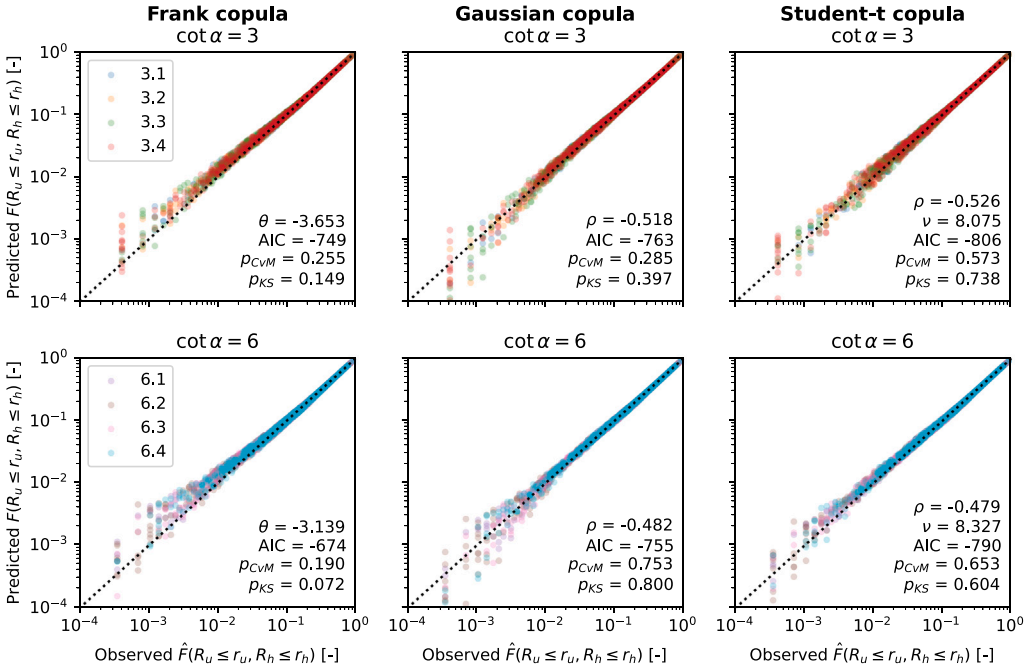

Fig. 12. Comparison of the cumulative probabilities from the empirical joint CDF and the CDF of the fitted Frank, Gaussian, and Student-t copulas, color-coded by experiment, for waterside slope angles of $\cot\alpha = 3$ (top) and $\cot\alpha = 6$ (bottom). A p_{CvM}-value and p_{KS}-value larger than 0.05 indicates a good fit.

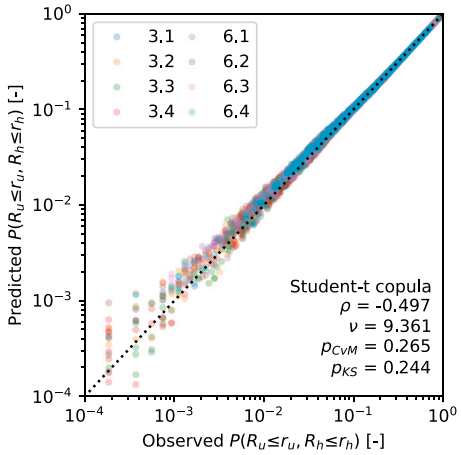

Fig. 13. Comparison of the cumulative probabilities of the empirical joint CDF and the CDF of the fitted Student-t copula, color-coded by experiment, independent on the waterside slope. A p_{CvM}-value and p_{KS}-value larger than 0.05 indicates a good fit.

6. Discussion

6.1. Variation in peak flow characteristics

This study investigated the variation and interdependency of peak flow characteristics in overtopping waves. The results showed that peak flow velocity (u_{peak}) and peak flow thickness (h_{peak}), conditional on the overtopping volume, exhibit significant variation. Moreover, u_{peak} and h_{peak}, conditional on the overtopping volume, are negatively correlated, implying that for any individual overtopping volume, an overtopping wave with a relatively high u_{peak} is more likely to correspond to a relatively low h_{peak}, and vice versa, see Fig. 15.

The variation of u_{peak} and h_{peak} and their interdependency has been previously studied, but has not yet been quantified for dikes. Hughes et al. (2012) examined $u_{peak,2\%}$ and $h_{peak,2\%}$ and their corresponding individual overtopping volumes and found that $u_{peak,2\%}$ and $h_{peak,2\%}$ did not occur within the same overtopping event. This study demonstrated that u_{peak} and h_{peak}, conditional on the overtopping volume, are negatively correlated. This aligns with Hughes et al. (2012), as a relatively high u_{peak} is more likely to be associated with a relatively small h_{peak}.

Mares-Nasarre et al. (2024) has analyzed the variation of u_{peak} and h_{peak} and their interdependency for overtopping flow at breakwater. Comparing this study focusing on dikes to their study on breakwaters shows different behavior of flow characteristics due to the experimental setups and methods. First, breakwaters have a rough, permeable cover layer, whereas dikes typically have a smooth, impermeable cover, which affects wave run-up and the overtopping flow. Second, Mares-Nasarre et al. (2024) conducted experiments on a shallow foreshore ($1.27 < d/H_s < 2.77$), while the FlowDike experiments focused on deep water ($3.33 < d/H_s < 6.11$). The shallow foreshore may cause the largest waves to break before reaching the breakwater, while waves on deep water break onto the dike. Lastly, the applied methods differ: Mares-Nasarre et al. (2024) analyzed the correlation between the absolute, dimensionless values of u_{peak} and h_{peak}, identifying a moderate positive correlation. In contrast, this study examines the correlation between their dimensionless residuals, conditional on overtopping volume, and finds a moderate negative correlation. These methodological differences make direct comparison between the studies challenging. Nevertheless, both identify a moderate correlation between u_{peak} and h_{peak} and demonstrate that their interdependency can be effectively modeled using copulas.

Another important flow characteristic of an overtopping wave is the overtopping time, T_{ovt}, which represents the duration of an overtopping event. Alongside u_{peak} and h_{peak}, T_{ovt} is used in erosion models by Dean et al. (2010) and van Bergeijk et al. (2021) to quantify the temporal aspect of erosion: how long the grass cover is subjected to the erosive forces exerted by the overtopping wave. As such, T_{ovt} is a key parameter for a time-dependent description of overtopping flow. Given a constant overtopping volume, a longer overtopping time is expected to result in lower values of either or both u_{peak} and h_{peak}, whereas a shorter overtopping time may lead to higher values. Although this study did not explicitly investigate T_{ovt}, a logical next step would be to incorporate it, alongside u_{peak} and h_{peak}, into a vine copula framework to investigate its influence on their variation and interdependency. For this purpose,

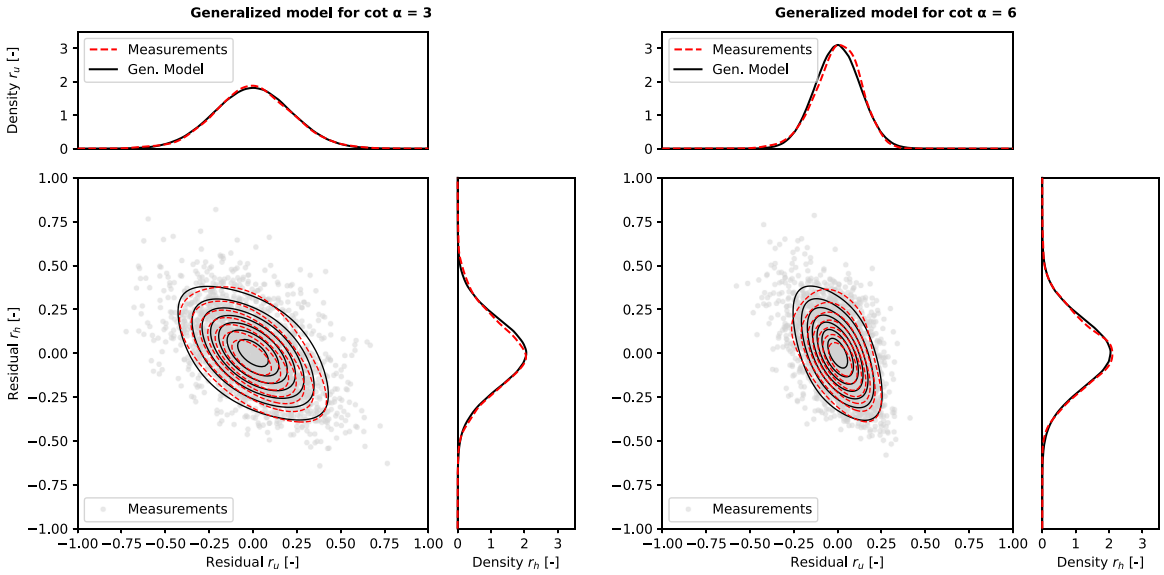

Fig. 14. Comparison between the residuals r_u and r_h from the FlowDike experiments (scatter/red dashed line), and the generalized model from this study (black line).

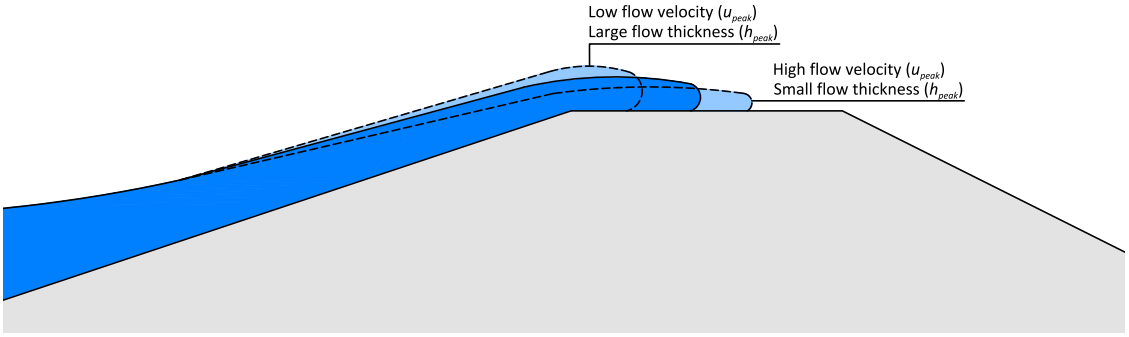

Fig. 15. Variation and interdependency of the peak flow characteristics of an overtopping wave lead to different overtopping flow patterns given the same overtopping volume.

estimates of T_{ovt} are needed, which can be obtained using methods proposed by other studies, such as Formentin and Zanuttigh (2019).

The variation and interdependency is quantified using log-transformed residuals and copula modeling, as it provided the best fit. As a result, the generalized model is more complex to implement and apply within erosion modeling. A simpler, albeit less accurate, approach is to use a bivariate normal distribution, while still assessing the variation and interdependency as function of the individual overtopping volume. Transforming the results into a bivariate normal distribution yields a coefficient of variation (COV) for u_{peak} of 23% and 13% for waterside slopes of 1:3 and 1:6, respectively. For h_{peak}, the COV is 20%, the correlation between u_{peak} and h_{peak} is −0.57. While the bivariate normal distribution provides a reasonable approximation, it slightly underestimates combinations near the center of the distribution and fails to capture tail dependence, leading to an overestimation of extreme event probabilities.

The variation of u_{peak} (σ_u) increases with a steeper waterside slope angle. One potential explanatory variable is the Iribarren number, which is smaller for the 1:6 waterside slope experiments ($\xi_{m-1,0} < 1.08$) compared to the 1:3 slope experiments ($\xi_{m-1,0} > 1.49$). A higher Iribarren number typically leads to more intense breaking and turbulence (Battjes, 1974b). However, the significant difference in σ_u between the two experiments, as shown in Fig. 7, suggests that the Iribarren number alone cannot account for this variation. Another possibility is the difference in distance along the slope between the breaking wave and the waterside crest line. However, the freeboard in the experiments with a 1:6 waterside slope is smaller than for the 1:3 waterside slope, resulting in a similar distance of approximately 30 cm, which makes this an unlikely cause. Lastly, the transition angle between the waterside slope and crest level could also play a role. For the steeper waterside slope, this transition is sharper, potentially increasing turbulence and air entrainment, which may lead to greater variation in u_{peak}.

The data used in this study are from small-scale experiments, which introduce some scale effects that need to be considered when analyzing the variation of u_{peak} and h_{peak}. Due to the smaller scale, the overtopping flow experiences more friction which leads to less overtopping water, as indicated by the Reynolds number. Additionally, surface tension plays a more significant role at small scales, affecting the wavefront by making it steeper, as explained by the Weber number. To minimize such scale effects, Heller (2011) recommends limit values of Re > 1000 and We > 10 for model studies. In total, approximately 85% of all individual overtopping events in the current dataset comply with both criteria. The remaining 15% consist of the smallest overtopping events, with a maximum dimensionless individual overtopping volume (V_T^*) of 0.19 (about 0.002 m^3/m). These smaller events are expected to exhibit minor scale effects, such as slightly increased turbulence and reduced surface tension at full scale, potentially leading to slightly greater variability. Nevertheless, since the Reynolds and Weber numbers are sufficiently large for the largest (and most relevant) overtopping waves to accurately capture turbulent flow behavior, overall scale effects are considered small. The largest individual overtopping volumes predominantly determine erosion, so the limited scale effects on smaller volumes have negligible impact on the overall application.

6.2. Model applicability

The generalized distributions and model proposed in Sections 5 and 3.4 are based on data from eight small-scale FlowDike experiments, each involving 400 to 900 individual wave overtopping events. This section discusses the applicable range of these models, which is largely defined by the experimental conditions listed in Table 1. Additionally, insights from other studies provide context for potential extrapolation beyond this range. The full application range of the generalized model is summarized in Table 5.

Four of the FlowDike experiments were conducted with a waterside slope of 1:3, and the other four with a slope of 1:6. A dependency between the waterside slope angle α and the variation of u_{peak} was identified, which is incorporated into the generalized distributions in Section 3.4 by defining the standard deviation as $\sigma_u(\alpha)$. Although the proposed distributions fit both waterside slopes well, they were calibrated only for these two specific angles, leaving the relation between σ_u and α unresolved.

Other studies have modeled the dependency between the expected value of u_{peak} and the waterside slope angle using expressions such as $1/\sin(\alpha)$ (Bosman et al., 2009), $1/\cot(\alpha)$ (van der Meer et al., 2011), and $\cot(\alpha)$ in a quadratic term (Formentin et al., 2019). However, van der Meer et al. (2012) identified inconsistencies among these approaches and instead proposed linear interpolation between two factors for the 1:3 and 1:6 slopes (EurOtop, 2018). Since none of these terms account for the factor of 1.77 difference between the σ_u values of the two slope angles, we propose a similar linear relation for σ_u, as given in Eq. (14). Additional validation for other waterside slope angles could refine this relation further.

For slopes shallower than 1:6, we propose using the 1:6 slope value as an upper limit, as σ_u decreases with decreasing slope angle. Conversely, for slopes steeper than 1:3, variation is likely to increase within the plunging wave regime ($\xi_{m-1,0} \lesssim 2.5$). However, for very steep slopes (e.g., steeper than 1:1.5), where waves transition to surging breakers ($\xi_{m-1,0} \gtrsim 3$), the flow may become more uniform again. The exact trend and magnitude remain uncertain, requiring further research.

$$\begin{aligned} \sigma_u(\alpha) &= 0.03\cot\alpha + 0.039 \quad \text{for} \quad 3 \le \cot\alpha \le 6 \\ \sigma_u(\alpha) &= 0.129 \quad \text{for} \quad \cot\alpha > 6 \end{aligned} \tag{14}$$

Between experiments, wave conditions were also varied. Since the experiments were conducted at a small scale, we use dimensionless parameters to define the applicable range of the model. For the relative freeboard R_c/H_{m0}, the range of values differs between the 1:3 and 1:6 waterside slopes, as shown in Section 3.3. Apart from the waterside slope, the change in σ_u over R_c/H_{m0} is minimal. For low relative freeboards ($R_c/H_{m0} \le 0.5$), a slight decrease in σ_h is observed, though the trend lines for both slopes align well. Therefore, we propose that the generalized model is applicable for $R_c/H_{m0} \ge 0.5$. For small relative freeboards, σ_h appears to decrease while σ_u remains constant, suggesting that the model could be applied as an upper limit.

The Iribarren number $\xi_{m-1,0}$ in the experiments ranged from 0.76 to 2.11, covering only plunging breakers. As shown in Section 3.3, the effect of $\xi_{m-1,0}$ on σ_u is minimal. A slight dependency appears for σ_h, showing a small increase in variation for Iribarren numbers between 1.0 and 1.5. The generalized model is calibrated for $0.76 < \xi_{m-1,0} < 2.11$, but could be applied with caution outside this range as long as plunging breakers are present ($0.2 - 0.5 \lesssim \xi_{m-1,0} \lesssim 2.5 - 3.0$). For non-breaking waves, the flow on the dike crest differs significantly (Guo et al., 2014; Formentin et al., 2019), requiring further research.

All experiments were conducted with normally incident waves. Wave obliqueness is not explicitly accounted for in the models used to calculate the expected values for u_{peak} or h_{peak}. Wave obliqueness and other effects like berms and roughness are incorporated into the wave run-up height of the overtopping volume distribution (van der Meer, 2002; EurOtop, 2018). Nevertheless, oblique waves could potentially influence variation. Since wave run-up and overtopping decrease as waves become more oblique (Oosterlo et al., 2021), we expect variation to decrease as well as we observed less variation for lower individual overtopping volumes (see Fig. 4). Therefore, we propose that the generalized model can be applied as an upper limit when considering oblique waves.

Table 5
Application range of the generalized distributions proposed in Section 3.4 and generalized model proposed in Section 5.

Parameter	Application range
Waterside slope angle ($\cot\alpha$)	$L3 \le \cot\alpha \le 6$ *As upper limit:* $\cot\alpha > 6$
Relative freeboard (R_c/H_{m0})	$R_c/H_{m0} \ge 0.5$ *As upper limit:* $0 < R_c/H_{m0} < 0.5$
Iribarren number ($\xi_{m-1,0}$)	$0.76 < \xi_{m-1,0} < 2.11$ *As upper limit:* $0.2 - 0.5 \lesssim \xi_{m-1,0} \lesssim 2.5 - 3.0$ (Plunging waves)
Obliqueness of waves	Normally incident waves *As upper limit:* Oblique waves
Dimensionless individual overtopping volume (V_T^*)	$V_T^* \le 2$ *With caution:* $2 < V_T^* \le 3$

The largest dimensionless individual overtopping volumes V_T^*/H_{m0} in this study were around 2, with outliers up to 3. For $H_{m0} = 1$ m, this corresponds to overtopping volumes of 2–3 m^3/s/m, and for $H_{m0} = 2$ m, 8–12 m^3/s/m. These values align with the maximum individual overtopping volumes reported in overtopping volume distributions, such as those by Hughes et al. (2012). When applying the proposed model, it is recommended to ensure that the dimensionless individual overtopping volume remains below 2, or with caution, at most 3.

6.3. Model application for erosion modeling

To demonstrate the implications of this study, we assess two fictional case studies that compare erosion modeling for a river and a sea dike, with and without the inclusion of variation and interdependency of the peak flow characteristics. The assumed geometry, water levels, and wave conditions for these case studies are shown in Fig. 16. For both cases, we calculate the expected erosion at the landward toe of the dike caused by a storm with 5000 incoming waves (N_w). The erosion modeling is based on an existing method described by van Bergeijk et al. (2021), which serves as the reference and is briefly outlined below.

The total number of overtopping waves (N_{ow}) is determined by assuming that wave run-up follows a Rayleigh distribution (Battjes, 1974a). This allows estimation of the overtopping probability (P_{ov}), which, when combined with N_w, yields N_{ow}. For each overtopping waves, the individual overtopping volume V_T is Weibull distributed (Hughes et al., 2012; Zanuttigh et al., 2014). By integrating the product of the probability of V_T with the calculated erosion caused by V_T, and then multiplying it with the number of overtopping waves N_{ow}, we find the expected erosion $E(D)$ during a storm, see Eq. (15).

$$E(D) = N_{ow} \int_0^{N_{ow}} f(V_T)\, D(V_T)\, dV_T \tag{15}$$

To calculate the resulting erosion for any V_T, we first need to determine the peak flow velocity u_{peak} and peak flow thickness h_{peak} at the waterside crest of a dike, for which several relations exists in literature (van der Meer et al., 2011; Hughes, 2017; Altomare et al., 2020). It is chosen to use (Hughes, 2017) as the relations are derived for dikes

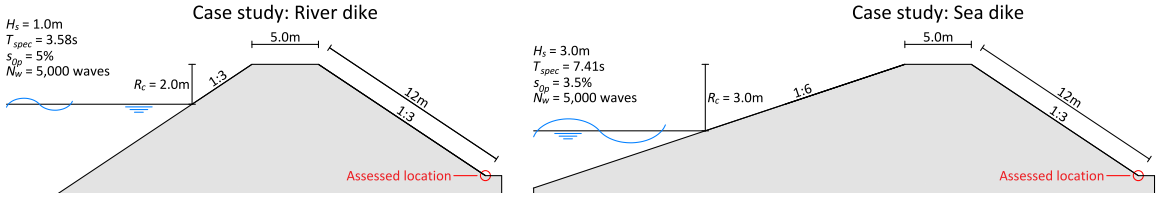

Fig. 16. Dike geometry, wave conditions and freeboard used in the case study of the river dike (left) and sea dike (right).

in deep water whereas van der Meer et al. (2011) is derived specifically for the wave overtopping simulator and Altomare et al. (2020) for shallow foreshores. At this point, the variation and interdependence of u_{peak} and h_{peak} is modeled using the generalized model described in Section 5. Then, using van Bergeijk et al. (2019), we translate the u_{peak} and h_{peak} along the crest and landward slope to determine the loading at the toe of the dike.

To model the erosion of the grass cover, we apply the cumulative overload method (COM) (van der Meer et al., 2011), which is a widely used approach for modeling dike erosion due to wave overtopping. In COM, the erosion rate is represented by the damage number (D), which depends on the shear stress exerted by overtopping waves exceeding the critical shear stress of the grass revetment. A simplified version of the COM is given in Eq. (16). The shear stress is assumed to be proportional to the square of the peak flow velocity (u_{peak}^2). The critical shear stress of the grass revetment is proportional to the square of the critical velocity (u_c^2), and depends on the grass cover condition. For an open sod, the deterministic value of u_c is approximately 4.3 m/s, whereas for a closed sod, it is about 6.6 m/s (van Hoven and van der Meer, 2017). For simplicity, we neglect the effects of the geometrical transition.

$$D = \sum_{i=0}^{N_{ow}} \max({u_{peak,i}}^2 - {u_c}^2; 0) \tag{16}$$

By combining Eq. (15) and Eq. (16), we obtain an erosion model that probabilistically assesses erosion at the landward toe of a dike. When variation and interdependency are not included, this method is similar in approach to existing methods like van Bergeijk et al. (2021). To quantify the effect of incorporating variation and interdependency in peak flow characteristics, we compare the expected damage number $E(D)$ for both cases where variation and interdependency are included and where they are excluded.

For both the river and sea dikes the results are shown in Table 6 and show that incorporating the variation and interdependency in peak flow velocity increases the expected damage number ($E(D)$) for grass erosion in all cases. The added uncertainty gives also insight in the standard deviation of the predicted $E(D)$. Furthermore, since shear stress scales with u_{peak}^2, the largest waves contribute most significantly to damage. When variation is not considered, these critical flow velocities occur only when a sufficiently large overtopping volume is exceeded. However, when variation is accounted for, high peak flow velocities can also arise due to the natural variability of smaller overtopping volumes. The effect is particularly significant in cases when the critical velocity is seldom exceeded, such as during small wave heights or strong grass revetments (e.g., the river dike scenario and closed sods).

Table 6
Expected damage number ($E(D)$) at the landward toe for a storm of 5,000 incoming waves, including and excluding the variation and interdependence of u_{peak} and h_{peak}.

Case	$E(D)$ for a storm (5,000 waves) [m^2/s^2]	
	Without variation	With variation
River dike		
Open sod	813.17	859.42 ($\sigma \approx 333.61$)
Closed sod	14.41	21.51 ($\sigma \approx 24.77$)
Sea dike		
Open sod	9650.00	9692.83 ($\sigma \approx 1432.64$)
Closed sod	1156.35	1189.53 ($\sigma \approx 358.98$)

7. Conclusion

The goal of this study was to quantify and model the variation and interdependency of the peak overtopping flow velocity (u_{peak}) and peak overtopping flow thickness (h_{peak} at the waterside crest line of a dike. With the shift toward design of dike crests heights using erosion modeling, erosion rates are now assessed based on individual overtopping volumes mostly in a probabilistic framework. To accurately model this erosion, a time-dependent description of the overtopping flow at the waterside crest line is essential. The u_{peak} and h_{peak} are critical boundary conditions in this context. Current relations for these characteristics rely on expected values derived from marginal distributions, neglecting both the variation and interdependency of u_{peak} and h_{peak}. This study is the first time that this variation and interdependency of u_{peak} and h_{peak} are quantified and modeled for dikes.

This study provides a detailed quantification of the variation and interdependency of u_{peak} and h_{peak}, conditional on the individual overtopping volume, using data from small-scale FlowDike experiments. The variation of u_{peak} and h_{peak} is quantified through residual analysis. We found that variation in u_{peak} increases with steeper waterside slopes, ranging from approximately 13% on a 1:6 slope to 23% on a 1:3 slope for plunging waves. In contrast, the variation in h_{peak} remained consistent across both slopes at around 20%.

The interdependency between u_{peak} and h_{peak} showed a moderate negative correlation, which we successfully modeled using a Student-t copula ($\nu = 9.361$, $\rho = -0.497$). The Student-t copula proved robust across both waterside slope angles. This negative correlation indicates that overtopping events with a relatively high u_{peak} are more likely to have a relatively low h_{peak}, and vice versa. This finding is significant, as it highlights that the variation in u_{peak} and h_{peak} cannot be treated independently without risking unrealistic representations of overtopping events.

The findings in this study can be applied within erosion models to improve the accuracy of erosion predictions by providing a more detailed representation of flow characteristics by overtopping waves. The addition of the variation and interdependency of u_{peak} and h_{peak} to these models leads to a more realistic relation between the peak flow characteristics, resulting in more of their natural variation. Additionally, the findings from this study offers valuable insights for the design of wave overtopping simulators, enabling more realistic simulations by integrating both variability and dependencies. The proposed methodology can be extended to other scenarios, such as steeper slopes ($\cot\alpha < 3$) or small relative freeboards ($R_c/H_{m0} < 0.5$), through further experimental analysis.

CRediT authorship contribution statement

Niels van der Vegt: Writing – review & editing, Writing – original draft, Visualization, Project administration, Methodology, Investigation, Formal analysis, Conceptualization. **Jord J. Warmink:** Writing – review & editing, Supervision, Methodology, Funding acquisition, Conceptualization. **Bas Hofland:** Writing – review &

editing, Supervision, Methodology, Funding acquisition, Conceptualization. **Vera M. van Bergeijk:** Writing – review & editing, Methodology, Conceptualization. **Suzanne J.M.H. Hulscher:** Writing – review & editing, Supervision, Methodology, Funding acquisition, Conceptualization.

Acknowledgments

The authors would like to thank Dr. Steven A. Hughes for providing the FlowDike dataset and his analysis of individual overtopping events. We also acknowledge the FlowDike team for their efforts in conducting the experiments.

This work is part of the Perspectief research programme Future Flood Risk Management Technologies for Rivers and Coasts with project number P21-23. This programme is financed by Domain Applied and Engineering Sciences of the Dutch Research Council (NWO).

Appendix A. List of symbols

Symbol	Description
α	Waterside slope angle [-]
$\xi_{m-1,0}$	Iribarren number based on $T_{m-1,0}$
σ_h	Standard deviation of residuals r_h [-]
σ_u	Standard deviation of residuals r_u [-]
d	Water depth at the toe of the dike [m]
f_s	Sampling frequency [Hz]
g	Gravitational acceleration constant (= 9.81) [m/s^2]
h	Overtopping flow thickness [m]
h_{peak}	Peak overtopping flow thickness [m]
$h_{peak,2\%}$	Peak overtopping flow thickness exceeded by 2% of the incoming waves [m]
h^*_{peak}	Dimensionless peak overtopping flow thickness [-]
H_{m0}	Significant wave height [m]
$L_{m-1,0}$	Wave length based on $T_{m-1,0}$ [m]
N	Number of incoming waves [-]
N_{ow}	Number of overtopping waves [-]
$T_{m-1,0}$	Spectral wave period [s]
T_p	Peak wave period [s]
q_{avg}	Average overtopping discharge [m^3/s/m]
r_h	Logarithmic transformed residuals of the h^*_{peak}, conditional on V^*_T [-]
r_u	Logarithmic transformed residuals of the u^*_{peak}, conditional on V^*_T [-]
R_c	Freeboard, difference between SWL and crest level [m]
R_u	Wave run-up height, relative to SWL [m]
$s_{m-1,0}$	Wave steepness based on $T_{m-1,0}$ [-]
u	Overtopping flow velocity [m/s]
u_{peak}	Peak overtopping flow velocity [m/s]
$u_{peak,2\%}$	Peak overtopping flow velocity exceeded by 2% of the incoming waves [m/s]
u^*_{peak}	Dimensionless peak overtopping flow velocity [-]
V_T	Individual overtopping volume [m^3/m]
V^*_T	Dimensionless individual overtopping volume [-]

Appendix B. Supplementary data

Supplementary material related to this article can be found online at https://doi.org/10.1016/j.coastaleng.2025.104772.

Data availability

All scripts used in this analysis are provided as Python notebooks and are available on GitHub: https://github.com/nielsvandervegt/overtopping_variation.

References

Altomare, C., Gironella, X., Suzuki, T., Viccione, G., Saponieri, A., 2020. Overtopping metrics and coastal safety: A case of study from the Catalan Coast. J. Mar. Sci. Eng. 8 (8), 556. http://dx.doi.org/10.3390/jmse8080556.

Battjes, J.A., 1974a. Computation of Set-Up, Longshore Currents, Run-Up and Overtopping Due to Wind-Generated Waves (Ph.D. thesis). Delft University of Technology, Delft, URL: http://resolver.tudelft.nl/uuid:e126e043-a858-4e58-b4c7-8a7bc5be1a44.

Battjes, J.A., 1974b. Surf similarity. In: Coastal Engineering 1974 - Conf. Proc. American Society of Civil Engineers, pp. 466–480. http://dx.doi.org/10.1061/9780872621138.029.

Bosman, G., van der Meer, J.W., Hoffmans, G., Schüttrumpf, H., Verhagen, H.J., 2009. Individual overtopping events at dikes. In: Coastal Engineering 2008 - Conf. Proc. World Scientific Publishing Company, pp. 2944–2956. http://dx.doi.org/10.1142/9789814277426_0244.

Dean, R.G., Rosati, J.D., Walton, T.L., Edge, B.L., 2010. Erosional equivalences of levees: Steady and intermittent wave overtopping. Ocean Eng. 37 (1), 104–113. http://dx.doi.org/10.1016/j.oceaneng.2009.07.016.

den Bieman, J., Doeleman, M., Smale, A., Mascini, M., 2024. Wave Run-Up Velocties. Derivation of an Expression to be used in the Cumulative Overload Method. Technical Report 11208057-037-GEO-0002, Deltares.

EurOtop, 2018. In: van der Meer, J.W., Allsop, N.W.H., Bruce, T., De Rouck, J., Kortenhaus, A., Pullen, T., Schüttrumpf, H., Troch, P., Zanuttigh, B. (Eds.), EurOtop 2018. Manual on Wave Overtopping of Sea Defences and Related Structures. An Overtopping Manual Largely based on European Research, but for Worldwide Application. Technical Report, EurOtop, www.overtopping-manual.com.

Fisher, R.A., 1992. Statistical methods for research workers. In: Breakthroughs in Statistics. Springer, New York, pp. 66–70. http://dx.doi.org/10.1007/978-1-4612-4380-9_6, ISBN: 978-1461243809.

Formentin, S.M., Gaeta, M.G., Palma, G., Zanuttigh, B., Guerrero, M., 2019. Flow depths and velocities across a smooth dike crest. Water 11 (10), http://dx.doi.org/10.3390/w11102197.

Formentin, S.M., Zanuttigh, B., 2019. Semi-automatic detection of the overtopping waves and reconstruction of the overtopping flow characteristics at coastal structures. Coast. Eng. 152, 103533. http://dx.doi.org/10.1016/j.coastaleng.2019.103533.

Guo, X., Wang, B., Liu, H., Miao, G., 2014. Numerical simulation of two-dimensional regular wave overtopping flows over the crest of a trapezoidal smooth impermeable sea dike. J. Waterw. Port Coast. Ocean. Eng. 140 (3), http://dx.doi.org/10.1061/(asce)ww.1943-5460.0000234.

Heller, V., 2011. Scale effects in physical hydraulic engineering models. J. Hydraul. Res. 49 (3), 293–306. http://dx.doi.org/10.1080/00221686.2011.578914.

Hughes, S.A., 2011. Adaptation of the Levee Erosion Equivalence Method for the Hurricane Storm Damage Risk Reduction System (HSDRRS). Technical Report, US Army Corps of Engineers - Engineer Research and Development Center, Vicksburg, MS, p. 142, URL: http://hdl.handle.net/11681/7717.

Hughes, S.A., 2015. Hydraulic Parameters of Individual Overtopping Wave Volumes. Technical Report, Colorado State University - Engineering Research Center, Fort Collins, CO, p. 68.

Hughes, S.A., 2017. Hydraulic parameters of overtopping wave volumes. In: Coastal Structures and Solutions To Coastal Disasters 2015 - Conf. Proc. American Society of Civil Engineers, pp. 710–718. http://dx.doi.org/10.1061/9780784480304.075.

Hughes, S.A., Thornton, C.I., 2016. Estimation of time-varying discharge and cumulative volume in individual overtopping waves. Coast. Eng. 117, 191–204. http://dx.doi.org/10.1016/j.coastaleng.2016.08.006.

Hughes, S.A., Thornton, C.I., van der Meer, J.W., Scholl, B.N., 2012. Improvements in describing wave overtopping processes. In: Coastal Engineering 2012 - Conf. Proc., vol. 3, Coastal Engineering Research Council, pp. 2085–2099. http://dx.doi.org/10.9753/icce.v33.waves.35.

ILIT, 2006. In: Seed, R.B., Bea, R.G., Abdelmalak, R.I., Athanasopoulos, A.G., Boutwell, G.P., Bray, J.D., Briaud, J.-L., Cheung, C., Cobos-Roa, D., Cohen-Waeber, J., Collins, B.D., Ehrensing, L., Farber, D., Hanemann, M., Harder, L.F., Inkabi, K.S., Kammerer, A.M., Karadeniz, D., Kayen, R., Moss, R.E.S., Nicks, J., Nimmala, S., Pestana, J.M., Porter, J., Rhee, K., Riemer, M.F., Roberts, K., Rogers, J.D., Storesund, R., Govindasamy, A.V., Vera-Grunauer, X., Wartman, J.E., Watkins, C.M., Wenk, Jr., E., Yim, S.C. (Eds.), Investigation of the Performance of the New Orleans Flood Protection Systems in Hurricane Katrina on August 29, 2005. Technical Report Volume I: Main Text and Executive Summary, Independent Levee Investigation Team, URL: https://usace.contentdm.oclc.org/digital/collection/p266001coll1/id/2932/.

Lorke, S., Bornschein, A., Schüttrumpf, H., Pohl, R., 2012a. FlowDike-D. Influence of Wind and Current on Wave Run-Up and Wave Overtopping. Technical Report, RWTH Aachen and TU Dresden, URL: http://resolver.tudelft.nl/uuid:73cb6cbe-8931-4499-b4d6-aa31548f5dda.

Lorke, S., Scheres, B., Schüttrumpf, H., Bornschein, A., Pohl, R., 2012b. Physical model tests on wave overtopping and flow processes on dike crests influenced by wave-current interaction. In: Coastal Engineering 2012 - Conf. Proc., vol. 2, Coastal Engineering Research Council, pp. 1770–1782. http://dx.doi.org/10.9753/icce.v33.waves.34.

Mares-Nasarre, P., Argente, G., Gómez-Martín, M.E., Medina, J.R., 2019. Overtopping layer thickness and overtopping flow velocity on mound breakwaters. Coast. Eng. 154, 103561. http://dx.doi.org/10.1016/j.coastaleng.2019.103561.

Mares-Nasarre, P., van Gent, M.R.A., Morales-Nápoles, O., 2024. A copula-based model to describe the uncertainty of overtopping variables on mound breakwaters. Coast. Eng. 189, 104483. http://dx.doi.org/10.1016/j.coastaleng.2024.104483.

Nagler, T., Vatter, T., 2024. pyvinecopulib: Python interface to vinecopulib. Version 0.7.1. URL: https://github.com/vinecopulib/pyvinecopulib.

Nelsen, R.B., 2006. An Introduction to Copulas. Springer Nature, ISBN 978-0387286594.

Oosterlo, P., Hofland, B., van der Meer, J.W., Overduin, M., Steendam, G.J., 2021. Field measurements of very oblique wave run-up and overtopping with laser scanners. J. Coast. Hydraul. Struct. http://dx.doi.org/10.48438/jchs.2021.0006.

Ponsioen, L., van Damme, M., Hofland, B., Peeters, P., 2019. Relating grass failure on the landside slope to wave overtopping induced excess normal stresses. Coast. Eng. 148, 49–56. http://dx.doi.org/10.1016/j.coastaleng.2018.12.009.

Schüttrumpf, H., Oumeraci, H., 2005. Layer thicknesses and velocities of wave overtopping flow at seadikes. Coast. Eng. 52 (6), 473–495. http://dx.doi.org/10.1016/j.coastaleng.2005.02.002.

Suzuki, T., Altomare, C., Yasuda, T., Verwaest, T., 2020. Characterization of overtopping waves on sea dikes with gentle and shallow foreshores. J. Mar. Sci. Eng. 8 (10), 752. http://dx.doi.org/10.3390/jmse8100752.

van Bergeijk, V.M., Verdonk, V.A., Warmink, J.J., Hulscher, S.J.M.H., 2021. The cross-dike failure probability by wave overtopping over grass-covered and damaged dikes. Water 13 (5), 690. http://dx.doi.org/10.3390/w13050690.

van Bergeijk, V.M., Warmink, J.J., Hulscher, S.J.M.H., 2022. The wave overtopping load on landward slopes of grass-covered flood defences: Deriving practical formulations using a numerical model. Coast. Eng. 171, 104047. http://dx.doi.org/10.1016/j.coastaleng.2021.104047.

van Bergeijk, V.M., Warmink, J.J., van Gent, M.R.A., Hulscher, S.J.M.H., 2019. An analytical model of wave overtopping flow velocities on dike crests and landward slopes. Coast. Eng. 149, 28–38. http://dx.doi.org/10.1016/j.coastaleng.2019.03.001.

van der Meer, J.W., 2002. Technical Report Wave Run-Up and Wave Overtopping at Dikes. Technical Report, Technical Advisory Committee on Flood Defence, URL: http://resolver.tudelft.nl/uuid:d3cb82f1-8e0b-4d85-ae06-542651472f49.

van der Meer, J., Hardeman, B., Steendam, G., Schüttrumpf, H., Verheij, H., 2011. Flow depths and velocities at crest and landward slope of a dike, in theory and with the wave overtopping simulator. In: Coastal Engineering 2010 - Conf. Proc., vol. 4, Coastal Engineering Research Council, pp. 2728–2742. http://dx.doi.org/10.9753/icce.v32.structures.10.

van der Meer, J.W., Provoost, Y., Steendam, G.J., 2012. The wave run-up simulator, theory and first pilot test. In: Coastal Engineering 2012 - Conf. Proc., vol. 5, Coastal Engineering Research Council, pp. 4069–4083. http://dx.doi.org/10.9753/icce.v33.structures.65.

van Gent, M.R.A., 2002. Low-Exceedance Wave Overtopping Events: Measurements of Velocities and the Thickness of Water-Layers on the Crest and Inner Slope of Dikes. Technical Report DC1-322-3, Delft Cluster, URL: http://resolver.tudelft.nl/uuid:e71289dd-f6aa-471e-856c-832071a83753.

van Hoven, A., van der Meer, J.W., 2017. Onderbouwing Kansverdelingen Kritisch Overslagdebiet Ten Behoeve Van OI2014v4 (Dutch) [Substantiation of Probability Distributions of Critical Overtopping Discharge for OI2014v4]. Technical Report 1230090-011-GEO-0006-jvm, Deltares, URL: http://resolver.tudelft.nl/uuid:d3cb82f1-8e0b-4d85-ae06-542651472f49.

Zanuttigh, B., van der Meer, J.W., Bruce, T., Hughes, S.A., 2014. Statistical characterisation of extreme overtopping wave volumes. In: From Sea to Shore – Meeting the Challenges of the Sea - Conf. Proc. ICE Publishing, pp. 442–451. http://dx.doi.org/10.1680/fsts.59757.048.

Zwillinger, D., Kokoska, S., 2019. CRC Standard Probability and Statistics Tables and Formulae. CRC Press, ISBN 978-0429181467.